Scalable, Nanometer-Accurate Fabrication of All-Dielectric Metasurfaces with Narrow Resonances Tunable from Near Infrared to Visible Wavelengths

Giulia Prone, Ute Drechsler, Christoph Mayr, Olga Semenova, Christine Thanner, Antonis Olziersky, Martin Eibelhuber, Marcel Mayor, and Emanuel Lörtscher*

Dielectric metasurfaces are a class of flat-optical elements that provide new ways to manipulate light. Irrespective of the underlying operation principle, the realization of such nanometer-sized structures requires a high fabrication accuracy, e.g., to match resonant conditions. While electron-beam lithography (EBL) achieves feature sizes below 10 nm, transparent substrates, as used for transmission devices, are challenging due to proximity effects. Furthermore, EBL's sequential exposure limits the exposable area, making it unaffordable for applications. Here, a novel fabrication route is described based on a master template created by EBL, which is then replicated by nanoimprint lithography (NIL). A three-layer process enables high-resolution nanoimprint resists with low etching selectivity with respect to semiconductors yet to be used. The resulting structures are highly reproducible and defect-free thanks to the selective removal of residual layers and a master not suffering from proximity effects. Exemplarily, elliptical Mie resonators are fabricated with tunable resonances from the near infrared (NIR) to the visible wavelength regime. They reveal a high uniformity and sensitivity toward dielectric changes. The generic fabrication approach enables upscaling of nanoscale metasurfaces to wafer scales by step-and-repeat techniques and deployment of the optical devices fabricated in real-world applications due to massively reduced costs.

1. Introduction

The ability to create optical elements at the nanometer scale has opened novel ways to manipulate light more efficiently and below the diffraction limit.[1,2] Among other concepts, metasurfaces are an emerging class of flat optical elements offering unprecedented opportunities for controlling light.[3,4] While plasmonic (mostly metallic) metasurfaces are driven by collective oscillations of the free charge carriers induced by an incident electromagnetic field, dielectric metasurfaces do not necessarily need free charge carriers as the underlying effects are different,[5] e.g., based on Mie resonances.[6] Whereas surface plasmon polaritons are widely used in applications (e.g., in microplate readers for biosensing and medical analytics by tracking shifts in the plasmon resonance upon binding of analytes by surface-bound receptors[7]), dielectric metasurfaces are less often employed as their underlying working principles require a higher accuracy to operate,[8] e.g., to match resonant conditions. While fabricating metasurfaces for the IR regime is still feasible by UV photolithography or EBL,[9] scaling the structures down to operate in the near-IR or even visible regime remained challenging as feature sizes below 10 nm are required. Moreover, besides performance gain over state-of-the-art technology, key to commercial success of novel devices in general and of metasurfaces in particular, are scalability, cost efficiency, and high-throughput manufacturing capabilities.

G. Prone, U. Drechsler, A. Olziersky, E. Lörtscher
IBM Research Europe – Zurich
Säumerstrasse 4, CH-8803 Rüschlikon, Switzerland
E-mail: eml@zurich.ibm.com

G. Prone, M. Mayor
Department of Chemistry
University of Basel
St. Johanns-Ring 19, CH-4056 Basel, Switzerland

The ORCID identification number(s) for the author(s) of this article can be found under https://doi.org/10.1002/adpr.202200014.

C. Mayr, O. Semenova, C. Thanner, M. Eibelhuber
EV Group
DI Erich Thallner Strasse 1, A-4782 Florian am Inn, Austria

M. Mayor
Karlsruhe Institute of Technology
Institute of Nanotechnology
P. O. Box 3640, D-76021 Karlsruhe, Germany

M. Mayor
Lehn Institute of Functional Materials (LIFM)
School of Chemistry Sun Yat-Sen
University Guangzhou
Guangdong 510275, China

Consequently, the efficiency of operation for such devices depends on the fabrication accuracy achieved. Hence, the geometrical dimensions should be controlled at the sub-10 nm level, ideally in all three dimensions, constituting very challenging requirements. Different mask-less, direct-write techniques such as direct laser writing (DLW), electron-beam lithography (EBL), focused ion-beam lithography (FIB), or scanning probe lithography (SPL) can be employed to create patterns with feature sizes below 10 nm.[10–12] In addition, extreme ultraviolet and interference lithography achieve similar feature sizes but use expensive masks and are limited in geometrical shapes. While DWL is limited in lateral resolution depending on the wavelength used, SPL can only pattern a few nms in depth at such high resolution which then requires an additional pattern transfer step to yield a higher topology. FIB in return suffers from damage in the target materials including ion channeling effects and generally a quite slow patterning speed. The biggest issue for EBL, however, is proximity effects, which will be discussed later. While every method offers specific advantages over others, common to all direct writing techniques is their sequential processing which limits upscaling to large areas or to a large number of samples, hence preventing mass-fabrication applications and widespread usage. While efforts to massively parallelize EBL by the interplay of multiple beams are ongoing,[13] EBL operation and fabrication costs are generally high, creating both physical as well as economical barriers. For typical exposures times of several tens of hours even for quite small areas (e.g., $1000 \times 1000\,\mu m$), the costs per sample exceed 1000 USD in realistic calculations. In addition to long EBL exposure times, the interactions of electrons with the resist and the substrate cause so-called electron proximity effects that lead to a deviation of the exposed and developed resist structures from the initial design.[14] While proximity correction algorithms based on point-spread functions or similar models are at the heart of modern EBL data preparation,[15,16] transparent, nonconductive substrates (as used mostly for transmission optics) are still difficult to handle because charge carriers are not drained and can accumulate inhomogeneously depending on structure density, stack, intensity, etc. To cope with proximity effects on nonconductive substrates, labor-intensive empirical test structures must be written for a stack with additional charge-draining layers before the design can be exposed appropriately, contributing again to the overall high costs.
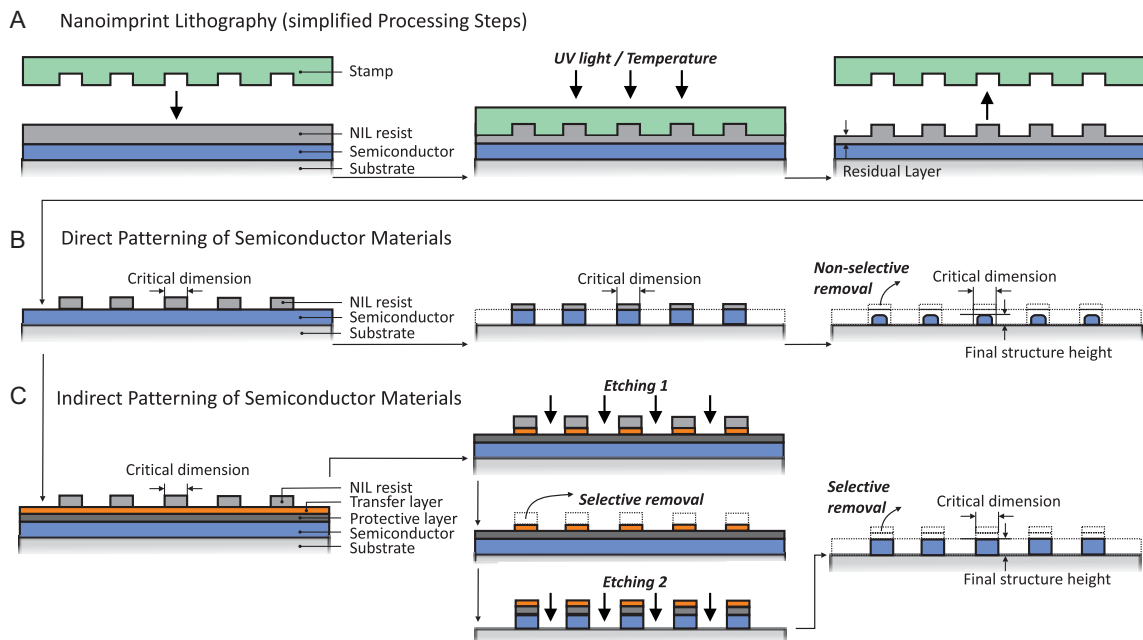
2. Conventional Nanoimprint Lithography

For the case where identical nanostructures are required either at various positions on the same target wafer or on multiple target wafers, an attractive method to fabricate structures in a more economical way compared to EBL (or any other direct-write nanostructuring method) alone is nanoimprint lithography (NIL),[17] based on seminal works performed in the 1990s.[18,19] NIL is based on transferring a master structure to a target substrate by imprinting. This process is repeatable and large areas can be patterned by step-and-repeat routines. NIL can be divided into three families: thermal NIL, ultraviolet (UV) NIL, and electrical NIL,[20] with UV NIL providing the highest resolution.[21] In **Figure 1**A the SmartNIL technology is employed, where a light-transparent mold is made from a master using a

UV-curable working stamp resin (EVG UV-NIL AS) on a flexible back-plane. Specifically, a photosensitive, acrylic imprint resist is coated on top of the target substrate and contacted at low pressure with the still liquid resist. The filling of the structures is predominantly driven by capillary forces. In this way, the resist conforms with the topology of the mold (Figure 1A, middle panel). The liquid resist is then cured upon exposure to UV light through the transparent mold, cross-linking the resist which yields a uniform, rigid polymer network. Next, the mold is separated (Figure 1A, right panel), leaving the negative topology of the working stamp in the resist behind. The target substrate can be processed further, e.g., in the simplest way, by a direct pattern transfer (Figure 1B) based on an etching step with the NIL resist acting as etching mask (Figure 1B, middle panel). For many material classes, the residual NIL resist can then be selectively removed (without affecting the target material), yielding the final structures (Figure 1B, right panel).

3. Three-layer Transfer

For the emerging class of all-dielectric metasurfaces, conventional NIL as described earlier has been deployed for the realization of perovskite nanometer gratings and nanohole arrays,[22] sub-100 nm wide Si_xN_y gratings,[13] epitaxial α-quartz nanopillars[23] or poly-Si meta-lenses,[24] mostly fabricated under high-throughput conditions as recently reviewed.[25] If the material to be patterned consists of Si, e.g., silicon-on-insulator[5] or silicon-on-glass, however, the conventional processing route cannot be used anymore without detrimentally affecting the semiconductor layer as the latter will be simultaneously removed or at least severely attacked by the cleaning etchants (e.g., SF_6). As a consequence, a direct pattern transfer (Figure 1B) is not directly applicable to dielectric metasurfaces. While some uniform feature-size reductions may potentially be tackled by design and labor-intensive efforts, a generic process is desirable. Before proposing such a process route, it should be noted that the master used for the molding can be made from any material that allows replication into a working stamp. That also includes high-conductive substrates that enable high-resolution EBL without causing proximity effects.

Motivated by the excellent scalability, resolution, and costs offered by NIL, a novel processing route[26] is proposed that enables high-performance NIL resists with low etching selectivity toward semiconductors still to be employed for patterning amorphous, microcrystalline, or crystalline semiconductors. The process is adapted from complementary metal–oxide–semiconductor (CMOS) manufacturing and is based on a three-layer system. Such a stack consists of the NIL layer, a transfer layer, and a protective layer on top of the semiconductor. The processing concept relies on first transferring the patterned NIL layer into the transfer layer, while subsequently enabling a selective removal of the NIL to resist thanks to the protection of the semiconductor by the protective layer. The transfer layer will further act as a hard mask to structure the protective layer. Last, the protective and transfer layers are used to pattern the semiconductor before selectively removing them. As a result, the semiconductor surface is entirely cleaned, and the lateral dimensions are not affected by nonselective etching. The

ADVANCED
SCIENCE NEWS
www.advancedsciencenews.com

ADVANCED
PHOTONICS
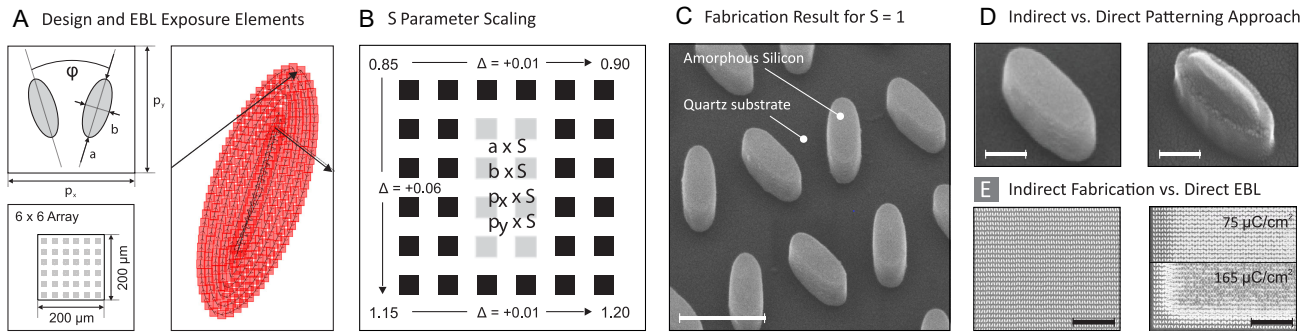**RESEARCH**
Open Access

www.adpr-journal.com

Figure 1. A) Simplified processing steps in nanoimprint lithography (NIL) using a stamp (fabricated from a master by molding; not shown) to pattern a NIL resist. When the stamp is contacted with the NIL-resist-coated substrate, depending on fluidic properties and structure dimensions, either external pressure or capillary forces drive the filling process. The transformation of the resist from liquid to solid phase can be achieved either by ultraviolet (UV) light or temperature, or a combination thereof. The residual layer is removed by non-selective etching (not shown). B) Direct transfer of NIL-fabricated resist structures into a semiconductor layer with unavoidable feature size and structure height reductions as well as surface roughening upon non-selective NIL resist removal. C) Indirect processing using a three-layer system; etching of a transfer layer, selective removal of the NIL resist without affecting the protecting and buried layers, opening of the protective layer, and final etching of the semiconductor layer with subsequent selective removal of the protective layer (without affecting the semiconductor layer). Compared to B), more accurate dimensions can be maintained as no feature-size and height reductions upon nonselective removal of the NIL resist take place. Further, as being protected, clean and defect-free surfaces and morphologies can be maintained.

concept of selective etching becomes evident when illustrating it with an example of its implementation; the protective layer can be composed of Al_xO_y, while the transfer layer may be SiO_2. The removal of the NIL layer is then done by SF_6 oxygen plasma (Figure 1C, middle panel) followed by cleaning under quite harsh conditions, which are applicable as the semiconductor is fully protected. The transfer into the semiconductor is then done by inductively coupled plasma reactive ion etching (ICP-RIE) (Figure 1C, middle panel) using a combination of the protective and transfer layers or only the protective one (after removing the transfer layer before). In principle, the generic process described can be used for transferring any nanopattern created with non-scalable and sequential lithographic methods to large areas and real-world applications using step-and-repeat approaches in NIL and the three-layer concept. Notably, other material stacks composed of different transfer, protective, and target layers than exemplarily described previously can be structured in a very similar manner using modified processing parameters or even different tools.

4. Fabrication of Elliptical Mie Resonators

As an example, we demonstrate the performance of the novel fabrication route for dielectric metasurfaces with respect to state-of-the-art direct patterning by the realization of all-dielectric, amorphous Si-based metasurfaces on a transparent quartz substrate. As a test system, pairs of tilted ellipses (**Figure 2**A; tilting angle $\phi = 35°$) were chosen as: 1) they demonstrate very narrow and highly tunable absorption features in the near infrared (NIR) regime,[27,28] and 2) ellipses are challenging and therefore benchmarking geometrical objects for any patterning technique beyond simple dots,[29] gratings[30] or rings.[31,32] In these ellipses, which constitute an array of nanoantennas, incident light excites magnetic and electric resonances–referred to as Mie resonances–that again translate into discrete peaks in the extinction spectrum. A high radiation efficiency and low conversion into heat are observed because of the low absorption loss of the dielectric material. As sub-wavelength dielectric resonators can support bound states in the continuum, the light is strongly confined, and sharp resonances (<10 nm full-width at half max (FWHM)) are consequently revealed. Their resonance frequencies depend on the specific geometry, constitutive material, and dielectric environment[33] rendering them interesting sensing elements with design-tunable spectral responses. Due to moderate filling factors, the ellipses arrays reveal smaller extinction coefficients than high-density, sub-wavelength metasurface gratings.[34] To showcase fabrication accuracy, the smallest deviations from the desired geometry will directly be visible in the optical spectra

Figure 2. A) Design of the unit cell (top left) of size p_x and p_y with a single pair of ellipses with long, a, and short, b, axes, being tilted by an angle ϕ. Ellipse filling (right) by electron-beam lithography (EBL) exposure elements starting from the edges and finishing at the center in a spiral path. Upscaling of single-pair ellipses to identical 6×6 arrays (bottom left). B) Uniform scaling of all ellipses' and unit cells' dimensions by the scaling parameter S, targeting an absorption resonance range from the near infrared (NIR ($S > 1.1$)) toward the visible range ($S < 1.0$). C) Example of ellipses fabricated for $S = 1.00$ (with $a = 280$ nm, and $b = 100$ nm, respectively; height: 100 nm) on a transparent quartz substrate (scaling bar: 300 nm). D) Comparison of indirect and direct patterning approaches for individual ellipses (scaling bars: 100 nm). E) Scanning electron microscope (SEM) images acquired at the corner of an array fabricated by the indirect process (left) versus directly patterned by EBL (at 20 kV) (right); the two nominal exposure doses indicated are both varied substantially towards the center of the array according to iterative, empirical electron proximity effect (PEC) corrections (scaling bars: 5 μm).

acquired. For EBL, tilted ellipse pairs with nanoscale dimensions further represent a challenge as the pattern generator has to work non-parallel to the two primary beam-deflection axes. In our approach, the ellipses were exposed using sub-field resolution units to place the exposure elements (exels). With this mode, a maximum exel-shot positioning accuracy can be achieved for these nonorthogonal shapes. The ellipse filling was performed by starting from the circumference and finishing at the center, following a spiral path. The writing order was from ellipse to ellipse across the whole pattern to reduce thermal drift effects (see arrows in the right panel of Figure 2A).

To showcase the benefits of our approach, we aimed at miniaturizing the geometries from the already reported NIR[35] to the visible wavelength regime using linear scaling of the unit cell and the dimensions of the ellipse (Figure 2A). Figure 2B depicts the scaling factors, S, ranging from 0.85 to 1.20 with $S = 1.00$ yielding $a = 280$ nm, and $b = 100$ nm, respectively (Figure 2A). The height of the a-Si was kept constant at 100 nm and also the angle between the ellipses, ϕ, was not varied. Figure 2C shows a sketch of the final ellipses arranged in an array. A single ellipse fabricated as described earlier (left), and one structured by direct pattern transfer (right) are depicted in Figure 2D. As it can be seen, the right one is still covered with residual NIL resist and suffers from defects and dimensional inaccuracies, in contrast to the near-perfect left one. For the entire array, the structures appear generally more uniform compared to direct EBL writing as the later process suffers from proximity effects (Figure 2E). This analysis will be shown next.
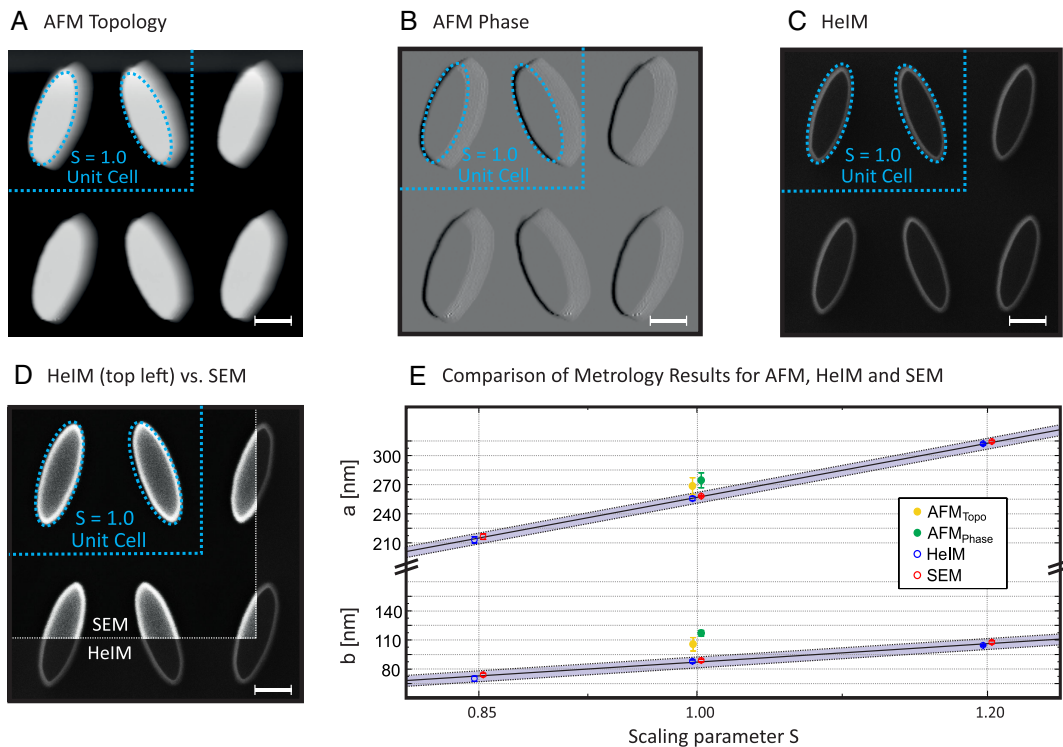
5. Metrology of Processing Results

Before reporting on the processing results, the metrological capabilities of three independent methods are assessed to characterize elliptical elements on transparent substrates; Atomic force microscopy (AFM), helium ion microscopy (HeIM), and scanning electron microscopy (SEM). **Figure 3** shows images acquired for the final processed sample with $S = 1.00$. When
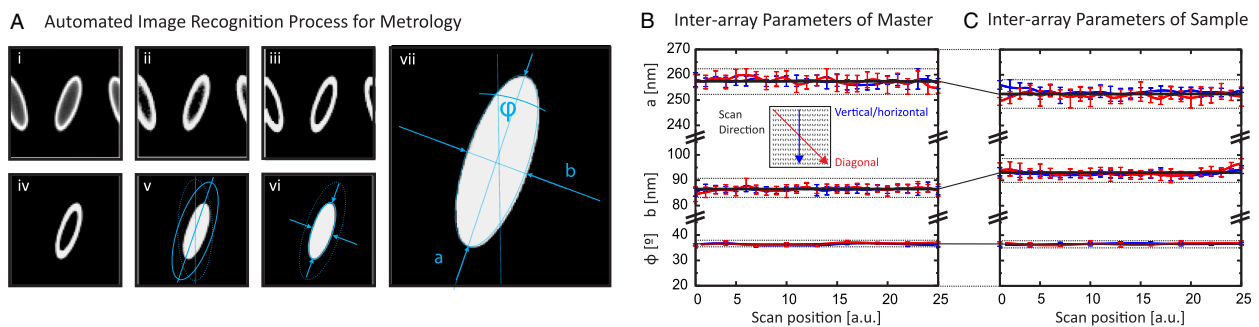
compared with the design geometry (including unit cell, cyan overlay), the structures appear too large in AFM topology irrespective of the mode used (e.g., tapping mode) (Figure 3A) most likely as a consequence of the finite tip radius (around 20 nm diameter) but also because of the step edges. The phase image (Figure 3B) confirms by the appearance of "shadows" that the tip is partially out-of-contact. Compared to AFM, the HeIM images are more accurate (Figure 3C) as the circumference can be clearly determined. For imaging, however, the samples had to be coated with 2 nm of platinum (Pt) to drain charges. Slightly more blurred edges appear in the SEM images (Figure 3D) both for the SE2 and the in-lens detector (on Pt-coated samples). The direct comparison with HeIM shows that the middle of the white-appearing edges in the SEM images should be taken as the physical boundary and that the measurement accuracy for SEM for the top metasurface edges is estimated to be around ± 2–5 nm. Hence, SEM is found to be capable of accurately measuring the dimensions of the elliptical metasurfaces, and will therefore be used for all metrology tasks in the following.

First, we assess the uniformity of individual metasurface elements across arrays of 200×200 μm (Figure 2A). This is an essential characterization as electron-induced proximity effects of densely packed structures usually affect the uniformity, leading to alternating dimensions of the structures inside the arrays compared to the ones located at or close to edges. For the highly geometry-sensitive metasurfaces, smallest deviations from the nominal dimensions will result in locally different optical behavior and broadened optical absorption features when averaged over a large area. Furthermore, inter-array uniformity is an important factor if large surfaces shall be created where all elements are intended to have identical optical properties. To determine the relevant parameters a and b for individual elements across the entire array, high-resolution SEM imaging is conducted along vertical/horizontal or diagonal line scans across an array (**Figure 4**A), followed by automated image recognition (flattening, binarization, single-object isolation, pattern matching) and parameter extraction as illustrated in Figure 4A. As

Figure 3. A) Comparison of metrology results for the final processed sample using atomic force microscope (AFM) topology, B) AFM phase, C) HeIM, or D) SEM (Scaling bars: 100 nm). E) Extracted values for the ellipses' main parameters, a and b, for three scaling values $S = 0.85$, 1.00, and 1.20, respectively. The purple lines show the linear geometry variation with consistent, slightly larger SEM values compared to HeIM.

Figure 4. A) Automated image recognition/processing steps by (i) converting a SEM raw image into a binary image (ii), applying an fast Fourier transform (FFT) filter (iii), removing border objects and filling open areas within the structures (iv). Finally, a pattern matching is performed using an ellipse shape to fit both angle (v) as well as long and short axes (vi), as depicted for the final processed image (vii). B) Inter-array parameters as determined for the Si master, and C) the processed sample for vertical/horizontal (blue trace), and diagonal (red trace) scan directions, respectively. The black lines represent the mean values of the entire scan trace.

the image recognition is based on an ellipse as the geometrical reference object and its angle is left as a degree of freedom for the pattern matching routine, the angle between the pair of ellipses can also be extracted and used as a measure to determine deviations from the perfect ellipse shape. To prevent charging upon SEM (at 3 kV), the final a-Si structures on quartz were coated with a uniform, 2 nm thin layer of Pt which is not needed for the high-conductive Si master. Figure 4B,C shows vertical/horizontal (blue) and diagonal (red) line scans representing measurements of eight ellipse pairs at each point for both Si master (B) and final
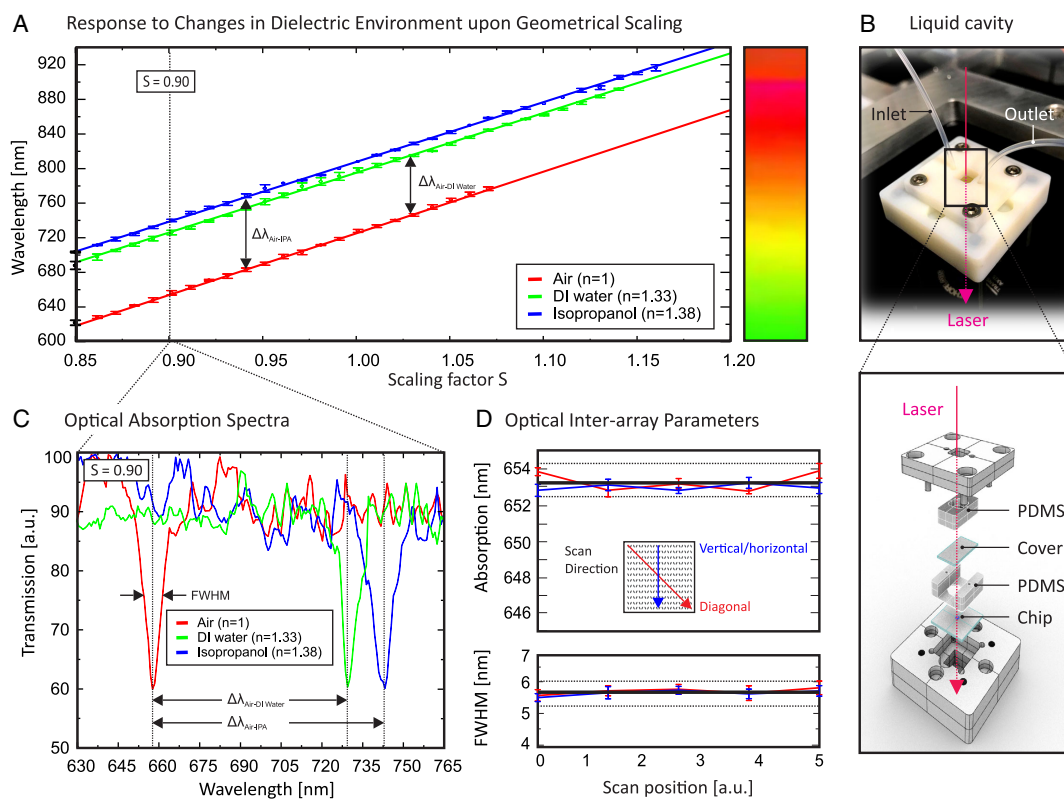
sample (C), respectively. For the Si master, $a = (257.5 \pm 4.5)$ nm, and $b = (86.3 \pm 2.8)$ nm is found, as well as $a = (252.5 \pm 4.6)$ nm and $b = (92.8 \pm 3.3)$ nm, for the final sample, respectively. The decrease of -5 nm for a and the increase of $+8$ nm for b upon replication can be explained by the volumetric shrinkage effects of the working stamp and the NIL resist when cross-linking. The result is a superposition of bulk and surface interactions. The root cause of the anisotropic behavior, however, is not yet revealed but found to be consistent and repeatable across all scaling values. Hence, the effect can be compensated by slightly

**ADVANCED
SCIENCE NEWS**

www.advancedsciencenews.com

**ADVANCED
PHOTONICS
RESEARCH**
Open Access

www.adpr-journal.com

adapting the master design. Looking at the scatter of all traces, no signs for proximity effects can be found within the measurement accuracy as more stochastic variations are revealed around the mean value, both for the Si master (deviation of ±4.0 nm around the mean value) as well as for the final sample (deviation of ±5 nm around mean value). Hence, the use of a high conductive substrate for EBL in combination with the novel indirect pattern transfer is found to yield high-accurate and uniform metasurfaces.

6. Optical Performance

A part from the geometrical properties of the metasurfaces, optical data is used to indirectly characterize the structures further. **Figure** 5C shows representative absorption resonances for $S = 0.9$, acquired in transmission (thickness of the quartz substrate 525 µm) under illumination with linearly polarized, broad-band light emitted from a tungsten lamp and the scattered and transmitted light collected with an objective and a spectrometer. The objective can further be manoeuvred over the sample by a piezoelectric stage allowing spot measurements to be taken. As a consequence of the small spot size (estimated to be <5 µm), the spectra are rather noisy but the number of metasurfaces acting actively as absorbers is finite. Looking at the red traces for

metasurfaces in air (dielectric index, $n = 1.00$), the FHWM of the resonances is around 6–8 nm with extinction factors of 30%–40%, both depending on the base line chosen. When plotting the resonances as a function of scaling factor S, a linear behavior is found (red curve in Figure 5A). The deviation from the linear fit is ±2.5 nm at maximum (red dotted lines; each data point representing three measurements over the entire array). When immersing the metasurfaces in a 200 µm thick cavity (Figure 5B) filled with a solution of distilled (DI) water ($n = 1.33$; conductivity = 0.059 µS cm^{-1}; green trace) or isopropanol (IPA; $n = 1.38$; blue trace), the absorption resonances shift by $\Delta\lambda$, as displayed in Figure 5C, with FWHM of 6–8 nm similar to the one measured in presence of air. Both shifts are consistent throughout all scaling factors with $\Delta\lambda_{air-IPA} = 80.5$–80.7nm, and $\Delta\lambda_{air-water} = 67.2$–67.4 nm, respectively. The deviation from the linear slope for the metasurfaces immersed in solvents increased slightly to ±9 nm (blue and green lines), most probably due to instabilities in the flexible Polydimethylsiloxane-glass cavity on top of the metasurfaces upon moving the stage. The figure of merit (FOM) to quantify and compare the optical response to dielectric changes in their environment is given by the ratio between the bulk sensitivity, $Sens_{bulk}$, and the FWHM. $Sens_{bulk}$ is given by the resonance shift, $\Delta\lambda$, divided by the dielectric index change, Δn: $S_{bulk} = \Delta\lambda/\Delta n = 67.3$ nm/ $(1.33-1.00) = 204$ nm refractive index unit^{-1} for the case

Figure 5. Optical characterization of metasurfaces: A) Scaling behavior of the resonance position as a function of S (varied from 0.85 to 1.20) and dielectric environment (air, DI water, and isopropanol). The scaling is found to be linear as expected. B) Liquid cavity with in- and outlets for medium exchange as well as explosion view thereof. C) Spectral absorption data for air (red data), DI water (green data), and isopropanol (blue data) as surrounding medium, exemplarily for $S = 0.9$. D) Inter-array uniformity of the absorption resonance positions (top) and FWHMs (bottom) along vertical/horizontal (blue data) and diagonal (red data) line scans.

air–Di water, and 212 nm refractive index unit^{-1} for the case air–IPA. With an average FWHM of 6.5 nm for air–water and 6.7 nm for air–IPA, the FOM yields 31.4, and 31.6, respectively. Similar to SEM metrology, the optical assessment of the interarray uniformity reveals very low variations in positions of the optical absorption resonances (±1.0 nm) and the FWHMs (±0.3 nm) across the entire array, as displayed in Figure 5D.

7. Conclusion

In conclusion, we demonstrated a novel fabrication route to create high-accurate (<10 nm) metasurfaces on transparent substrates that were geometrically scaled in resonance behavior from the NIR to the visible wavelength range. These devices, combined with a scalable and mass-fabrication compatible fabrication route, represent a formidable opportunity to leverage the unique optical properties of Si-based metasurfaces, such as their narrow and sensitive resonances, for various applications. Our processing approach allows cost-effective samples, which are roughly 2–3 orders of magnitude lower in price compared to EBL processing alone, to be fabricated by combined EBL and NIL, and which can fully compete with nonscalable fabrication approaches on the nanometer scale. The narrow resonances of elliptical metasurfaces with FWHMs of 6–8 nm represent a tunable, inherent spectroscopic feature that is attractive as an optical filtering structure or sensing substrate. For the latter and in combination with narrow light sources, it would enable bulky and expensive NIR and visible range detectors to be replaced by inexpensive CMOS imagers, suited for mobile applications. The novel fabrication route presented is generic to other geometries, different material stacks, other operation principles, and applications beyond optics and metasurfaces. The process can be realized with masters created by any nanopatterning method, including EBL, and is upscalable to large areas by step-and-repeat techniques.

8. Experimental Section

Master Fabrication: A Raith (Vistec) EBPG5200 EBL system with an acceleration voltage of 100 kV has been used under ultra-silent conditions to expose a 93 nm thick HSQ resist on a Si wafer. Standard silicon wafers were cleaned (oxygen plasma and surpass 3000 soaking) prior to HSQ 4% resist two-step spin coating. After EBL, the wafers were developed with AZ351B, etched with inductively-coupled plasma (ICP), and cleaned by oxygen plasma, buffered hydrofluoric acid (BHF), and piranha.

Quartz Wafer Preparation: Quartz wafers were coated with the three-layer system. First, plasma-enhanced chemical vapor deposition (PECVD) has been used to deposit 100 nm a-Si. Second, via atomic-layer deposition (ALD) plasma Oxford system a 12 nm protective layer Al_2O_3 has been realized (300°C). Finally, in Step 3 again PECVD has been used to deposit the 50 nm transfer layer of SiO_2 with a deposition rate of 43.4 nm min^{-1}.

NIL Post-processing: After NIL, the pattern transfer has been performed. The residual layer has been removed with ICP, then the etching of the three layers has been performed, respectively: 50 nm SiO_2 with RIE, Al_2O_3 with RIE, Al_2O_3 and a-Si with ICP. Finally, a BHF dip is performed to remove the remaining SiO_2/Al_2O_3.

Optical Characterization: A Newport Q-Series quartz tungsten halogen lamp 66 877 with 100 W and ≈850 lm flux has been used to acquire in transmission the absorption resonances. Before illuminating the sample, the broad-band light has been linearly polarized using a Glan–Taylor Polarizer, 10 mm Clear Aperture, Coating, 650–1050 nm. Spectra have been acquired by an Ocean Optics QEPro spectrometer with back-thinned Si CCD, TEC cooled, and sensitivity from 400 to 1100 nm. The light has been collected with an Olympus LMPLFLN100× objective, 100× magnification, 0.86 numerical aperture, and 3.4 mm working distance. The objective is equipped with a piezoelectric stage to have a further degree of freedom, allowing spot measurements to be taken.

Conflict of Interest

The authors declare no conflict of interest.

Data Availability Statement

The data that support the findings of this study are available from the corresponding author upon reasonable request.

[1] N. I. Zheludev, Y. S. Kivshar, *Nat. Mater.* **2012**, 11, 917.

[2] W. Cai, U. K. Chettiar, A. V. Kildishev, V. M. Shalaev, *Nat. Photonics* **2007**, 1, 224.

[3] H.-H. Hsiao, C. H. Chu, D. P. Tsai, *Small Methods* **2017**, 4, 1600064.

[4] N. Yu, F. Capasso, *Nat. Mater.* **2014**, 13, 139.

[5] J. W. J. Wang, *Chin. Opt. Lett.* **2018**, 16, 050006.

[6] M. V. Rybin, K. L. Koshelev, Z. F. Sadrieva, K. B. Samusev, A. A. Bogdanov, M. F. Limonov, Y. S. Kivshar, *Phys. Rev. Lett.* **2017**, 119, 24.

[7] J. Zhang, L. Zhang, W. Xu, *J. Phys. D: Appl. Phys.* **2012**, 45, 113001.

[8] P. Genevet, F. Capasso, F. Aieta, M. Khorasaninejad, R. Devlin, *Optica* **2017**, 4, 139.

[9] V.-C. Su, C. H. Chu, G. Sun, D. P. Tsai, *Opt. Express* **2018**, 26, 13148.

[10] A. Tseng, K. Chen, C. Chen, K. Ma, *IEEE Trans. Electron. Packag. Manuf.* **2003**, 26, 141.

[11] S. Cabrini, A. Carpentiero, R. Kumar, L. Businaro, P. Candeloro, M. Prasciolu, A. Gosparini, C. Andreani, M. D. Vittorio, T. Stomeo, E. D. Fabrizio, *Microelectron. Eng.* **2005**, 78, 11.

[12] A. A. Tseng, A. Notargiacomo, T. P. Chen, *J. Vac. Sci. Technol. B* **2005**, 23, 877.

[13] Y. Yao, Y. Wang, H. Liu, Y. Li, B. Song, W. Wu, *Appl. Phys. A* **2015**, *121*, 399.

[14] L. Ren, B. Chen, *IEEE* **2004**, *1*, 579.

[15] R. Murali, D. K. Brown, K. P. Martin, J. D. Meindl, *J. Vac. Sci. Technol. B* **2006**, *24*, 2936.

[16] R. Wüest, P. Strasser, M. Jungo, F. Robin, D. Erni, H. Jäckel, *Microelectron. Eng.* **2003**, *67*, 182.

[17] H. Schift, *J. Vac. Sci. Technol. B* **2008**, *26*, 458.

[18] S. Y. Chou, P. R. Krauss, P. J. Renstrom, *Appl. Phys. Lett.* **1995**, *67*, 3114.

[19] S. Y. Chou, P. R. Krauss, P. J. Renstrom, *Science* **1996**, *272*, 5258.

[20] M. C. Traub, W. Longsine, V. N. Truskett, *Annu. Rev. Chem. Biomol. Eng.* **2016**, *7*, 583.

[21] S. Gilles, M. Meier, M. Prömpers, A. van der Hart, C. Kügeler, A. Offenhäusser, D. Mayer, *Microelectron. Eng.* **2009**, *86*, 661.

[22] S. V. Makarov, V. Milichko, E. V. Ushakova, M. Omelyanovich, A. C. Pasaran, R. Haroldson, B. Balachandran, H. Wang, W. Hu, Y. S. Kivshar, A. A. Zakhidov, *ACS Photonics* **2017**, *4*, 728.

[23] Q. Zhang, D. Sánchez-Fuentes, R. Desgarceaux, P. Escofet-Majoral, *ACS Appl. Mater. Interfaces* **2019**, *12*, 4732.

[24] G.-Y. Lee, J.-Y. Hong, S. Hwang, S. Moon, H. Kang, S. Jeon, H. Kim, J.-H. Jeong, B. Lee, *Nat. Commun.* **2018**, *9*, 4562.

[25] D. K. Oh, T. Lee, B. Ko, T. Badloe, J. G. Ok, J. Rho, *Front. Optoelectron.* **2021**, *14*, 229.

[26] U. Drechsler, E. Lörtscher, P201906800US01 **2020**.

[27] M. Liu, D.-Y. Choi, *Nano Lett.* **2019**, *18*, 8062.

[28] F. Yesilkoy, E. R. Arvelo, Y. Jahani, M. Liu, A. Tittl, V. Cevher, Y. Kivshar, H. Altug, *Nat. Photonics* **2019**, *13*, 390.

[29] P. Spinelli, M. Verschuuren, A. Polman, *Nat. Commun.* **2012**, *3*, 692.

[30] C. Mateus, M. Huang, L. Chen, C. Chang-Hasnain, Y. Suzuki, *IEEE Photonics Technol. Lett.* **2004**, *16*, 1676.

[31] Y. Yang, I. I. Kravchenko, D. P. Briggs, J. Valentine, *Nat. Commun.* **2014**, *5*, 5753.

[32] A. I. Kuznetsov, A. E. Miroshnichenko, M. L. Brongersma, Y. S. Kivshar, B. Luk'yanchuk, *Science* **2016**, *354*, 6314.

[33] A. A. Komar, D. N. Neshev, A. E. Miroshnichenko, *JETP Lett.* **2017**, *106*, 709.

[34] Y. Yao, H. Liu, Y. Wang, Y. Li, B. Song, R. P. Wang, M. L. Povinelli, W. Wu, *Opt. Express* **2016**, *24*, 15362.

[35] A. Tittl, A. Leitis, M. Liu, F. Yesilkoy, D.-Y. Choi, D. N. Neshev, Y. S. Kivshar, H. Altug, *Science* **2018**, *360*, 1105.